Self-assembled α-MnO₂ urchin-like microspheres as a high-performance cathode for aqueous Zn-ion batteries

Yunzhao Wu, Ye Tao, Xianfu Zhang, Kai Zhang, Shengbin Chen, Yu Liu, Yong Ding[*], Molang Cai, Xuepeng Liu and Songyuan Dai[*]

ABSTRACT Aqueous Zn-ion batteries (AZIBs) are one of the promising battery technologies for the green energy storage and electric vehicles. As one attractive cathode material for AZIBs, α-MnO₂ materials exhibit superior electrochemical properties. However, their long-term reversibility is still in great suspense. Considering the decisive effect of the structure and morphology on the α-MnO₂ materials, hierarchical α-MnO₂ materials would be promising to improve the cycle performance of AZIB. Here, we synthesized the α-MnO₂ urchin-like microspheres (AUM) *via* a self-assembled method. The porous microspheres composed of one-dimensional α-MnO₂ nanofibers with high crystallinity, which improved the surface area and active sites for Zn^{2+} intercalation. The AUM-based AZIB realized a high initial capacity of 308.0 mA h g^{-1}, and the highest energy density was 396.7 W h kg^{-1}. The kinetics investigation confirmed the high capacitive contribution and fast ion diffusion of the AUM. *Ex-situ* XRD measurement further verified the synergistic insertion/extraction of H$^+$ and Zn^{2+} ions during the charge/discharge process. The superiority of the AUM guaranteed good electrochemical performance and reversible phase evolution, and this application would promote the follow-up research on the advanced AZIB.

Keywords: aqueous Zn-ion batteries, α-MnO₂ urchin-like microspheres, fast ion diffusion coefficients, reversible phase evolution, synergistic H$^+$-Zn^{2+} insertion/extraction

INTRODUCTION

Aqueous Zn-ion batteries (AZIBs) are one of the promising technologies for the green energy storage and electric vehicles. Typically, AZIBs consist of an intercalation-type cathode, a zinc metal anode and a Zn^{2+}-based aqueous electrolyte, which demonstrate attractive features of large theoretical capacity (820 mA h g^{-1} and 5855 mA h cm^{-3}), wide working potential window (0–2 V), reversible plating/stripping of Zn, high safety, environmental friendliness, low cost and facile manufacturing process [1–4]. Since Kang's group [5] developed the first prototype of AZIB in 2012, various manganese oxide materials have been intensively studied, such as MnO, α-MnO₂, β-MnO₂, γ-MnO₂, δ-MnO₂, λ-MnO₂, Mn₂O₃, Mn₃O₄ and Mn₂O₇ [6–9]. Among them, the α-MnO₂-based AZIBs exhibit the highest specific capacity of more than 380 mA h g^{-1}, long-term reversibility and extraordinary rate capability, which benefit from their 2×2 tunnel structure with corner-sharing double MnO₆ octahedra chains [10]. However, further commercialization of the α-MnO₂-based AZIBs is still restricted by the irreversible structural transformation and the dissolution of Mn^{2+} ions in the electrolyte during cycling.

Up to date, many efforts have been made to improve the cycle stability of the α-MnO₂ materials, including adding MnSO₄ into the electrolyte and protecting the surface of α-MnO₂ [11]. For example, Lian *et al.* [12] introduced the gradient Ti doping on the surface of the α-MnO₂ nanowires, and achieved the Zn/MnO₂ batteries with excellent high-rate capability and ultralong cycling stability. Other similar studies like the α-MnO₂@C [13] and α-MnO₂@In₂O₃ [14] also improved the cycling stability and rate performance of the α-MnO₂-based AZIBs. The aforementioned studies mainly focused on the protection of the α-MnO₂ nanowires itself, which was high-cost and low-efficiency in the scale-up application. Therefore, it is highly desirable to develop more practical

method that can realize high-performance and long-durable α-MnO$_2$-based AZIBs. Current research of the α-MnO$_2$ materials reveals that their electrochemical properties lie on the crystalline structure, morphology, and particle size of the α-MnO$_2$ [7]. Especially, the bulk structure with porous morphology can improve the electrical conductivity, specific surface area and inside pores of the active materials [15–19]. Thus, the fabrication of α-MnO$_2$ materials with hierarchical morphology is driving the interest of researchers [20,21]. The α-MnO$_2$ materials with hierarchical structures are ideal cathode materials to improve the cycle stability of the AZIBs.

Here, we synthesized the α-MnO$_2$ urchin-like microspheres (AUMs) *via* a self-assembled hydrothermal method, which were used as the cathode materials of AZIBs. The urchin-like microspheres were constructed by one-dimensional (1D) α-MnO$_2$ nanofibers, which improved the surface area and active sites for Zn^{2+} insertion/extraction. The AUM-based AZIBs achieved a high initial capacity of 308.0 mA h g^{-1}, and still maintained at 243.6 mA h g^{-1} after 200 cycles. The long cycle capacity retention was 170.2 mA h g^{-1} with a high Coulombic efficiency of 100% after 1000 cycles at 1000 mA g^{-1}. The highest energy density was 396.7 W h kg^{-1} at the power density of 129 W kg^{-1}. Based on the electrochemical and kinetics investigation, the AUM cathode showed a high capacitive contribution, as well as the fast ion diffusion coefficients during the charge/discharge process. The fast ion kinetics of the AUM cathode enabled the reversible phase evolution along with the synergistic insertion/extraction of H$^+$ and Zn^{2+} ions during the long-term cycling. This report of the AUMs would promote the follow-up research on the advanced cathode materials for AZIBs.

EXPERIMENTAL SECTION

Synthesis of the AUM

The AUMs were synthesized *via* a self-assembled method, including a chemical precipitation reaction followed with a hydrothermal treatment. Firstly, solution A was prepared by mixing 1.5 mmol MnSO$_4$·H$_2$O and 1 mL concentrated H$_2$SO$_4$ in 40 mL deionized water, and kept at 60°C. Secondly, 1.0 mmol KMnO$_4$ was dissolved in 10 mL deionized water to form solution B. Then, solution B was added dropwise into solution A with constant stirring, and the MnO$_x$ precipitation was formed immediately. After that, the mixture containing the MnO$_x$ templates was transferred to a Teflon-lined autoclave, and underwent a hydrothermal treatment set at 120°C for 10 h. At

last, the resulted AUM were collected, washed thoroughly with deionized water, and dried in an oven at 80°C.

Material characterization

The Smartlab SE instrument (Rigaku, Japan) was used to test the powder X-ray diffraction (XRD) patterns of the AUM powder. The scanning electron microscopy (SEM) images were obtained from a field-emission microscope (Quattro S, Thermo Fisher Scientific, USA). The transmission electron microscopy (TEM) and high resolution TEM (HRTEM) morphologies were observed by a field-emission JEM-2100 microscope (JEOL, Japan). X-ray photoelectron spectroscopy (XPS) was investigated on the K-Alpha instrument (Thermo Fisher Scientific, USA). Raman spectra were obtained from a home-built microscope with a 533 nm laser. The Brunauer-Emmett-Teller (BET) surface area and pore size distribution were obtained by a TriStarII3020 V1. 03 (Micromeritics Instrument Corp.).

Electrochemical measurements

The ZIBs were assembled into CR2025 coin-type cells. To fabricate the cathode, a slurry was prepared by mixing the AUM powders, acetylene black and polyvinylidene difluoride (PVDF) with a mass ratio of 80:10:10 in *N*-methyl-2-pyrrolidone (NMP). Then the slurry was coated on a stainless-steel foil with a mass loading of 1.0–1.5 mg cm^{-2}. The prepared cathode film was dried in an oven at 120°C for 12 h. The glass fiber membrane was used as the separator, a Zn foil as the anode, and an aqueous solution of 2 mol L^{-1} ZnSO$_4$ with 0.1 mol L^{-1} MnSO$_4$ as the electrolyte. Cyclic voltammetry (CV) tests with different scanning rates of 0.1–3.0 mV s^{-1}, galvanostatic charge-discharge (GCD) curves at various current densities of 100–3000 mA g^{-1} and electrochemical impedance spectroscopy (EIS) measurements in the frequency ranging from 0.01 to 10^5 Hz were conducted on an electrochemical workstation (CHI660D, Shanghai Chenhua Instruments Co., Ltd.). A CT2001A instrument (Wuhan LAND electronics Co., Ltd) was used to obtain the cycle and rate performances of the ZIBs. The diffusion coefficients of Zn^{2+} ions were analyzed by the galvanostatic intermittent titration technique (GITT) on the Zive Sp1 workstation (ZIVELAB, Korea).

RESULTS AND DISCUSSION

The AUMs were fabricated *via* a self-assembled method, which consisted of two steps of a chemical precipitation and a hydrothermal reaction. At the first step, a redox reaction between MnSO$_4$ and KMnO$_4$ occurred in the

H_2SO_4 solution, and the sphere-like MnO_x templates precipitated immediately. As shown in Fig. S1, the MnO_x agglomerates were 0.5–2 µm in dimension, and abundant nanoplates overgrew on the porous surface. XRD pattern (Fig. S2) revealed the relatively low crystallinity of the MnO_x composites, and the broad peaks matched with the α-MnO_2 (JCPDS # 44-0141). In the second step, the MnO_x templates were transferred to the autoclave to undergo a hydrothermal reaction at 120°C for 10 h. As a result, the MnO_x templates further crystalized and turned into nanofibers, meanwhile the nanofibers self-assembled into the urchin-like morphology. As shown in Fig. 1, the as-prepared AUM samples were 4–10 µm in dimension, and these interweaved α-MnO_2 nanofibers showed two kinds of morphology due to the varied sizes of the MnO_x templates. The bigger AUMs were urchin-like microspheres with hollow cavity (Fig. 1a–c), while the smaller AUMs were radiating agglomerates of the α-MnO_2 nanofibers (Fig. 1d–g). Such porous morphology could enlarge the specific surface area and inside pores of the active materials [22,23], and thus promote the insertion/extraction of Zn^{2+} ions from the electrolyte.

Further material characterizations were taken to investigate the AUM samples. Fig. 1h shows the crystal orientation of the α-MnO_2 nanofibers, which are the (211) plane in length and the (310) plane in width. The SAED images in Fig. 1i revealed the diffraction spots of (310), (400), (420), (521) and (710) planes, and the corresponding XRD diffraction peaks (Fig. 2a) matched well with the tetragonal α-MnO_2 (JCPDS # 44-0141). Raman spectrum also identified the v_3 and v_2 vibrations of the Mn–O bonds [19,24,25], located at 576.0 and 644.4 cm^{-1}, respectively (Fig. 2b). XPS data were further collected to analyze the elemental oxidation states in the AUM samples. The Mn 2p core level spectrum was deconvoluted into the Mn^{3+} and Mn^{4+} peaks, and the calculated contents of Mn^{3+} and Mn^{4+} in the AUMs were 16.2% and 83.8%, respectively (Fig. 2c). The co-existence of Mn^{3+} and Mn^{4+} atoms on the surface of the AUMs revealed high reaction activity of the α-MnO_2 nanowires. The high oxidation state of Mn was further confirmed by the large energy separation of Mn 3s spectral splitting (Fig. 2d), which originated from the exchange coupling between the 3s hole and the 3d electrons in Mn atom. Moreover, the splitting peak centered at 92 eV might be caused by the $3d^5$ configuration of Mn^{2+} ions [26]. In Fig. 2e, the O 1s
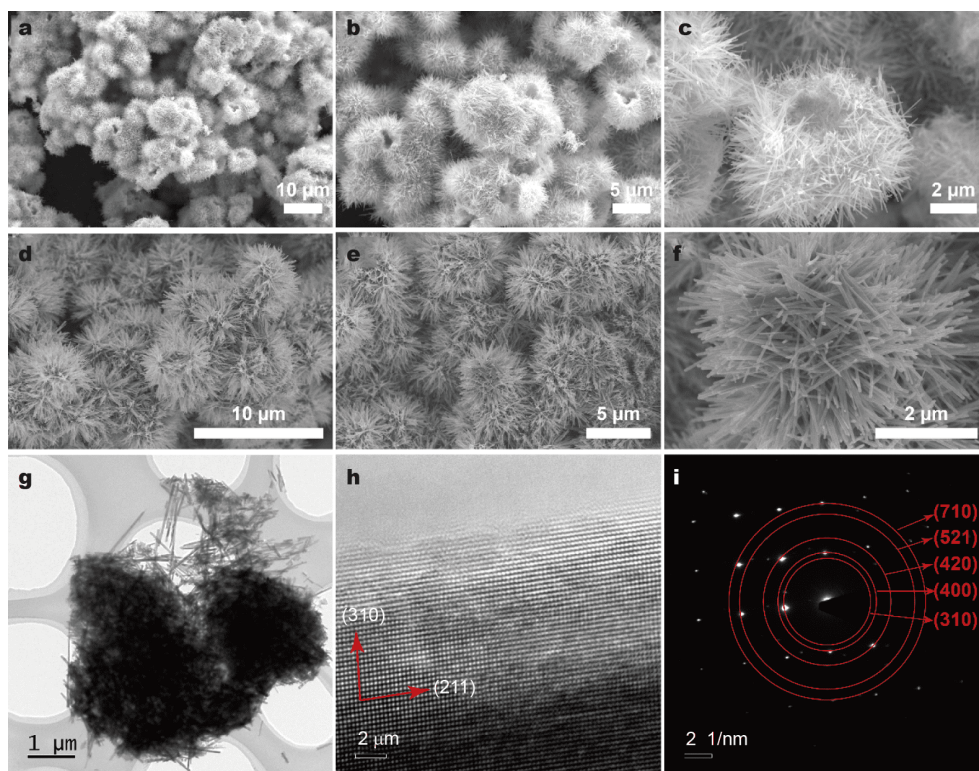

Figure 1 (a–f) SEM images of the as-prepared AUMs. (g) TEM, (h) HRTEM and (i) selected area electron diffraction (SAED) images of the α-MnO_2 nanofibers from the AUM samples.
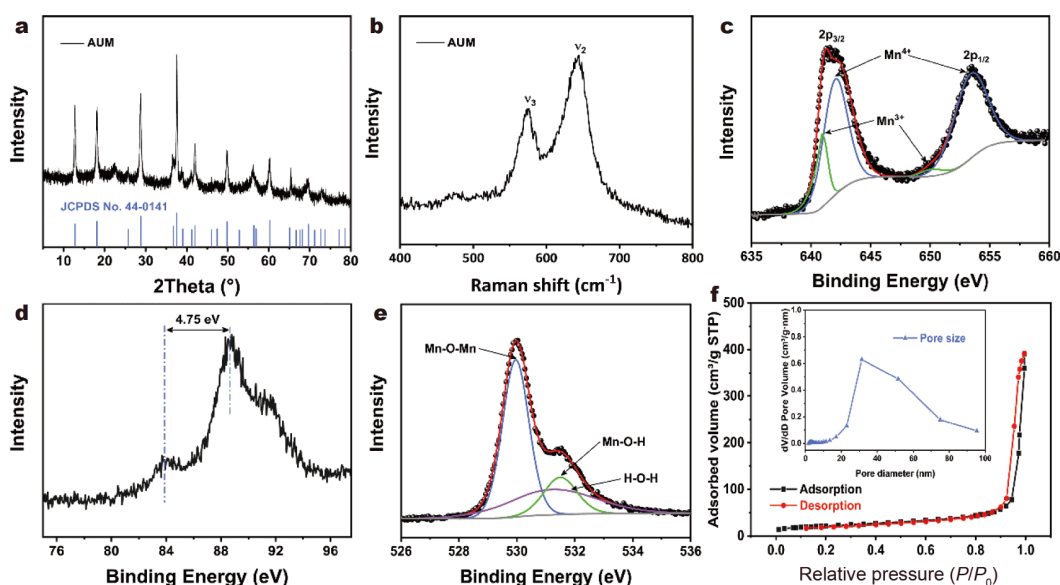
Figure 2 (a) XRD pattern, (b) Raman spectrum, (c) Mn 2p, (d) Mn 3s and (e) O 1s core-level XPS spectra and (f) nitrogen adsorption-desorption isotherms of the AUM samples, and the inset is the Barrett-Joyner-Halenda (BJH) pore-size distributions.

spectrum revealed the high contents of Mn–O–H bonds and H–O–H bonds, which were the evidence of the adsorbed water existing in the crystal structure [27,28]. Considering the synergistic insertion/extraction of H^+ and Zn^{2+} ions into the α-MnO_2, the adsorbed water would contribute to the electrochemical performances of the AUM-based AZIBs [29]. As shown in Fig. 2f and Fig. S3, the BET surface area of the AUMs was calculated to be 127.7 m^2 g^{-1}, which was much higher than that of the independent α-MnO_2 nanowires (37.8 m^2 g^{-1}). The high surface area and mesoporous structure of the AUMs provide the superior potential as the cathode materials for the ZIBs.

The electrochemical properties of the AUM-based ZIBs were exhibited in Fig. 3. The coin-type ZIBs were assembled by the AUM cathode, the Zn foil anode and 2 mol L^{-1} $ZnSO_4$ with 0.1 mol L^{-1} $MnSO_4$ as the electrolyte. As shown in Fig. S4, the α-MnO_2 nanowires on the AUMs were fully filled with the carbon black and maintained the microsphere structure. Such hierarchical structure could improve the electrical conductivity and electrochemical activity of the cathode materials, and accelerate the insertion/extraction of Zn^{2+} ions in the α-MnO_2 crystal. In Fig. 3a, the first five cycles of the AUM cathode were tested at 0.1 mV s^{-1}, and the reversible cathodic and anodic peaks were located at 1.39, 1.30, 1.56, 1.60 V, respectively. Fig. 3b, c show the rate performance and the corresponding GCD curves at different current densities of 100–3000 mA g^{-1}. The AUM-based batteries

achieved a high initial discharge capacity of 308.0 mA h g^{-1} at 100 mA g^{-1}, and maintained at 257.6, 228.2, 180.0, 142.8 and 121.6 mA h g^{-1} at 300, 500, 1000, 2000 and 3000 mA g^{-1}, respectively. After the rate tests, the battery capacity recovered to 295.3 mA h g^{-1} at 100 mA g^{-1} with the Coulombic efficiency of 99.3%. Moreover, the highest energy density (based on the cathode active mass) of the AUM-based batteries was 396.6 W h kg^{-1} at a power density of 128.8 W kg^{-1}, and the largest power density was 3813.6 W kg^{-1} at an energy density of 154.6 W h kg^{-1}. As illustrated in Fig. 3d and Table S1, the performance of the AUM cathode was very competitive compared with many reported α-MnO_2 materials and other cathode materials of AZIBs, including α-MnO_2 nanowires [29], α-MnO_2@TiO_2 [12], α-MnO_2@C nanoparticles [13], α-MnO_2 nanorods/CNTs composites [30], β-MnO_2 [31], Mn_2O_3@ppy [32], MnO_x@$Ti_3C_2T_x$ [33], $ZnMn_2O_4$@graphene [34], $ZnMn_2O_4$@PEDOT [35], $Na_{0.44}MnO_2$ [36], Na_xMnO_2 [37], V_2O_5 [38], $V_5O_{12}\cdot6H_2O$ [28], $Li_xV_2O_5\cdot nH_2O$ [39] and FeHCF [40]. As for the long cycle performance, the AUM-based batteries achieved the reversible capacities of 243.6 mA h g^{-1} after 200 cycles (100 mA g^{-1}) and 170.2 mA h g^{-1} after 1000 cycles (1000 mA g^{-1}), as well as the high Coulombic efficiencies of 99.2% and 99.9%, respectively (Fig. 3e, f). SEM images in Fig. S5 and XRD results in Fig. S6 also verified the cycle stability of the AUM cathode after long-term charging/discharging application. Such attractive rate performance and cycle properties verified the superiority
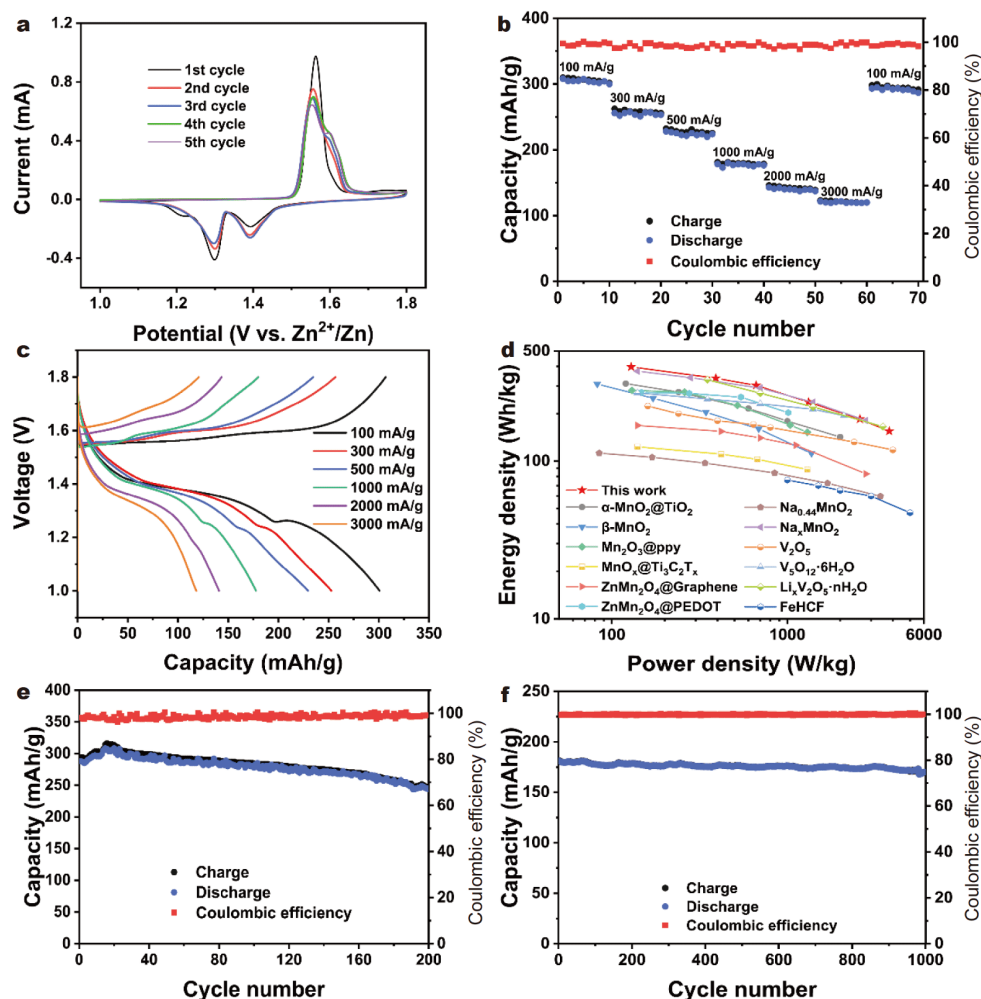
Figure 3 (a) CV curves of the AUM cathode tested at 0.1 mV s^{-1}. (b) Rate performance and (c) GCD tests at different current densities of 100–3000 mA g^{-1} of the AUM-based batteries. (d) Ragone plots of the AUM-based batteries compared with other cathode materials. Cycle performance of the AUM-based batteries at (e) 100 mA g^{-1} and (f) 1000 mA g^{-1}.

of the AUMs as the cathode materials for the AZIBs.

The charge storage mechanism of the AUM-based ZIBs was further investigated *via* the kinetics measurements in Figs 4 and 5. Based on $i_{pc} = av^b$, the peak current i_{pc} in the CV curves (Fig. 4a) meets a logarithmic relationship with the scanning rate v, and the value b is determined by the fitted slop of the log(i_{pc})-log(v) plots (Fig. 4b). The resulting value b of the C-peak 1, C-peak2, D-peak 3 and D-peak 4 were 0.71, 0.86, 0.79 and 0.58, respectively. These values over 0.5 indicated the charge storage process was capacity-controlled rather than diffusion-controlled [24,25]. The calculated percentages of capacitive contribution increased from 55.1% to 79.5% with the scanning rates improving from 0.1 to 1.0 mV s^{-1} (Fig. 4c). Such high capacitive contribution can be attributed to the

improved electrical conductivity and electrochemical activity due to the porous surface and hollow structure of the AUM cathode (Fig. S4), which could accelerate the insertion/extraction of Zn^{2+} ions in the α-MnO$_2$ crystals.

Further analyses of the ion diffusion kinetics were conducted *via* the EIS and GITT. Fig. S7 shows the EIS plots measured at different discharge states of 1.4 and 1.2 V. Based on the Equations (S1 and S2), the calculated diffusion coefficients of the electrodes at 1.4 and 1.2 V were 4.15×10^{-10} and 5.11×10^{-11} cm^2 s^{-1}, respectively (Fig. 4d). Such one magnitude distinction revealed the different diffusion kinetics during the discharge process. As shown in Fig. 5, the D values for the charge and discharge process were in the range of 10^{-6}–10^{-10} and 10^{-7}–10^{-12} cm^2 s^{-1}, respectively. The fast ion diffusion
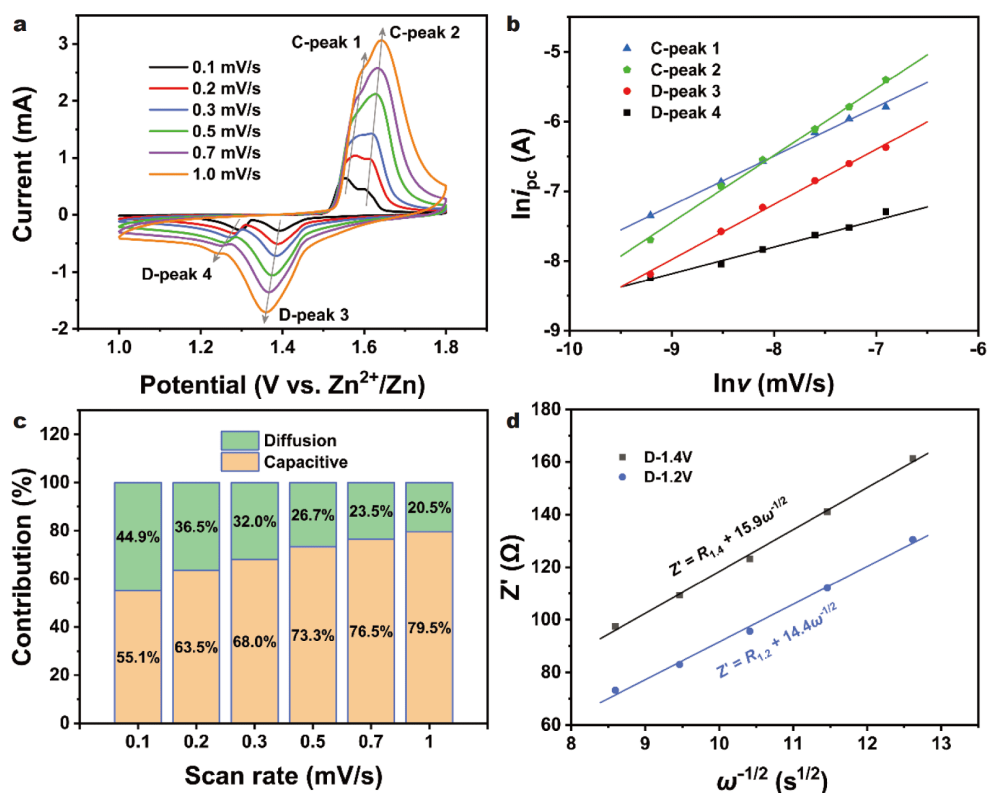
Figure 4 (a) CV curves of the AUM cathode at various scanning rates of 0.1–1 mV s^{-1}. (b) Linear fitting of the *b* value derived from the CV curves. (c) Contents of the capacity-controlled and diffusion-controlled contribution in the charge storage process. (d) Linear fitting of the *Z'*-$\omega^{-1/2}$ relationships obtained from the EIS data.
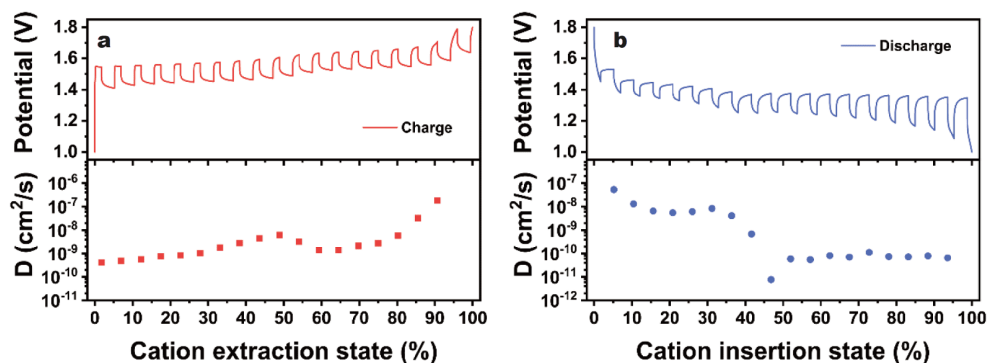

Figure 5 GITT curves and the corresponding diffusion coefficients (*D*) of the AUM-based ZIBs measured in (a) the charge process and (b) the discharge process.

kinetics further verified the superiority of the AUMs as the cathode materials for the AZIBs. In addition, a significant watershed of the *D* values appeared at 1.3 V for the discharge process, which was consistent with the EIS measurement in Fig. 4d. This phenomenon demonstrated that different ion diffusion behaviors existed in the discharge process.

Further structural analyses of the AUM cathode during the charge/discharge process are illustrated in Fig. 6, Fig. S8 and Table S2. A typical GCD profile (Fig. 6a) of the AUM-based ZIBs is marked with seven dots (named I-VI), and the corresponding XRD patterns are illustrated in Fig. 6b. Table S2 reveals that the diffraction peaks of the AUMs (I and II) shift to higher angles due to the
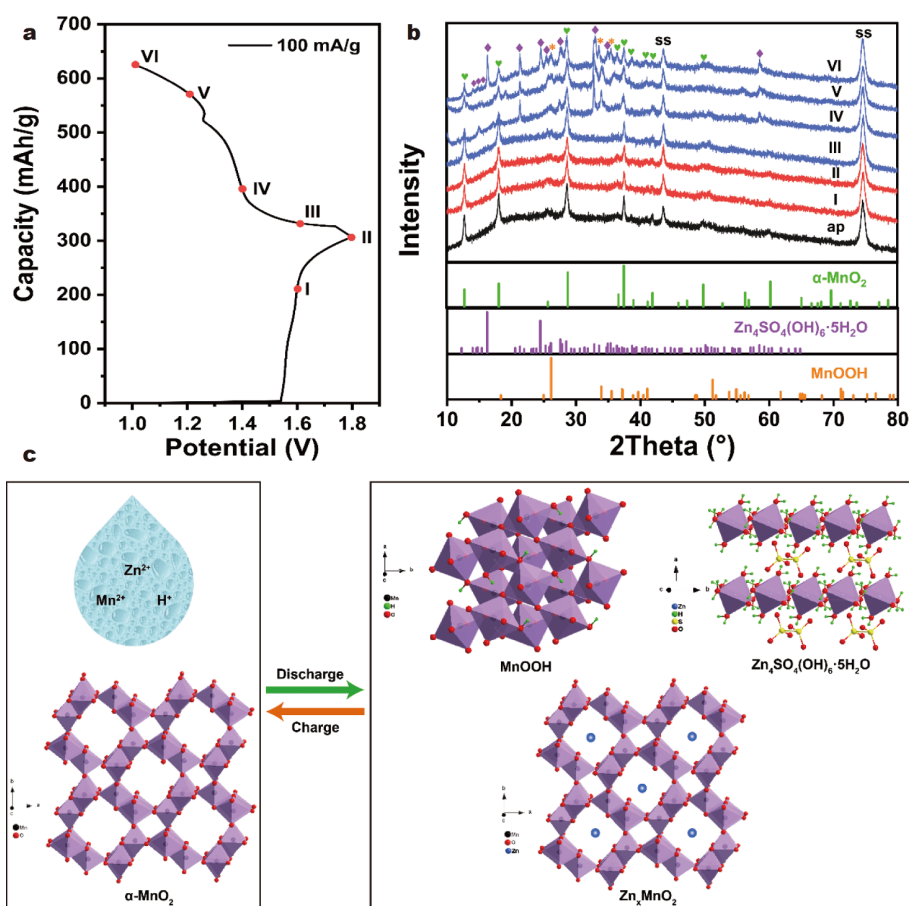
Figure 6 (a) The GCD curves of the AUM-based ZIBs at 100 mA g^{-1}. (b) *Ex-situ* XRD patterns of the AUM cathodes at different charge/discharge states. (c) The charge storage mechanism of the AUM cathode during the charge/discharge process.

extraction of Zn^{2+} ions during the charge process, and no impurity signals appear at the end of the charge process. When the AUM electrode was discharged to 1.0 V, there was a distinct difference in the XRD results before and after the watershed point (1.3 V). As the AUM electrodes discharged below 1.3 V (V and VI), two new phases emerged in the XRD patterns, which matched with the MnOOH (JCPDS # 41-1437) and Zn$_4$SO$_4$(OH)$_6$·5H$_2$O (JCPDS # 39-0688). Recently, a synergic intercalation/ extraction mechanism of the H$^+$ and Zn^{2+} ions in the AZIBs was reported, which considered the diffraction peaks of the MnOOH and Zn$_4$SO$_4$(OH)$_6$·5H$_2$O phase as a solid proof [41–43]. In our case, the H$^+$-resulted phase appeared in the XRD patterns during the charge and discharge process, which gave a clear scheme of the structural evolution during the charge/discharge process (Fig. 6c). When the AUM cathode was discharging, the Zn^{2+} ions inserted into the 2×2 tunnel of the α-MnO$_2$ with the accompany of the H$^+$ ions, and the MnOOH and

Zn$_4$SO$_4$(OH)$_6$·5H$_2$O phase formed due to the pH value increment of the electrolyte near the cathode. In Fig. S8, the interplanar spacing of the (310) and (210) planes increased from 0.310 and 0.241 nm to 0.321 and 0.247 nm, respectively, which proved the insertion of Zn^{2+} ions into the α-MnO$_2$. During the charge period, the extraction of the H$^+$ and Zn^{2+} ions proceeded with the dissolution of the MnOOH and Zn$_4$SO$_4$(OH)$_6$·5H$_2$O phase. As a result, the structural transition of the urchin-like microspheres was reversible with the synergic inter-calation/extraction of the H$^+$ and Zn^{2+} ions during the charge/discharge process. In addition, the morphology and structural characterization of the AUM cathode after cycling (Figs S5, S6) further proved the cycle stability of this AUM cathode material.

CONCLUSION
In summary, we developed the self-assembled AUMs as the cathode material for AZIBs. The typical procedure

consisted of a chemical precipitation and a hydrothermal reaction. The resulting AUMs were porous spheres (5–10 μm in dimension) with two kinds of morphologies due to the varied sizes of the MnO_x templates. The bigger AUMs were urchin-like microspheres with hollow cavity, while the smaller AUMs were radiating agglomerates of the α-MnO_2 nanofibers. The assembled AUM-based ZIBs achieved high initial capacity of 308.0 mA h g^{-1}, and maintained at 243.6 mA h g^{-1} after 200 cycles. The long cycle capacity retention was 170.2 mA h g^{-1} with a high Coulombic efficiency of 100% after 1000 cycles at 1000 mA g^{-1}. The highest energy density was 396.7 W h kg^{-1} at the power density of 129 W kg^{-1}. Such rate performance and cycle stability verified the superiority of the AUM as the cathode material for the AZIBs. In addition, the electrochemical kinetics investigation revealed the high capacitive contribution and the fast ion diffusion coefficients of the AUM cathodes. *Ex-situ* XRD measurement further verified the synergistic insertion/extraction of H^+ and Zn^{2+} ions during the charge/discharge process, which guaranteed the reversible phase evolution of the AUM structure. This application of the AUMs would promote the follow-up research on the advanced ZIBs.

1   Song M, Tan H, Chao D, et al. Recent advances in Zn-ion batteries. Adv Funct Mater, 2018, 28: 1802564

2   Wan F, Niu Z. Design strategies for vanadium-based aqueous zinc-ion batteries. Angew Chem Int Ed, 2019, 58: 16358–16367

3   Song WJ, Lee S, Song G, et al. Stretchable aqueous batteries: Progress and prospects. ACS Energy Lett, 2019, 4: 177–186

4   Tang B, Shan L, Liang S, et al. Issues and opportunities facing aqueous zinc-ion batteries. Energy Environ Sci, 2019, 12: 3288–3304

5   Xu C, Li B, Du H, et al. Energetic zinc ion chemistry: The rechargeable zinc ion battery. Angew Chem Int Ed, 2012, 51: 933–935

6   Hu Y, Wu Y, Wang J. Manganese-oxide-based electrode materials for energy storage applications: How close are we to the theoretical capacitance? Adv Mater, 2018, 30: 1802569

7   Konarov A, Voronina N, Jo JH, et al. Present and future perspective on electrode materials for rechargeable zinc-ion batteries. ACS Energy Lett, 2018, 3: 2620–2640

8   Wu Y, Wang M, Tao Y, et al. Electrochemically derived graphene-like carbon film as a superb substrate for high-performance aqueous Zn-ion batteries. Adv Funct Mater, 2020, 30: 1907120

9   Wu Y, Zhang K, Chen S, et al. Proton inserted manganese dioxides as a reversible cathode for aqueous Zn-ion batteries. ACS Appl Energy Mater, 2019, 3: 319–327

10 Wu B, Zhang G, Yan M, et al. Graphene scroll-coated α-MnO_2 nanowires as high-performance cathode materials for aqueous Zn-ion battery. Small, 2018, 14: 1703850

11 Fang G, Zhou J, Pan A, et al. Recent advances in aqueous zinc-ion batteries. ACS Energy Lett, 2018, 3: 2480–2501

12 Lian S, Sun C, Xu W, et al. Built-in oriented electric field facilitating durable Zn-MnO_2 battery. Nano Energy, 2019, 62: 79–84

13 Islam S, Alfaruqi MH, Song J, et al. Carbon-coated manganese dioxide nanoparticles and their enhanced electrochemical properties for zinc-ion battery applications. J Energy Chem, 2017, 26: 815–819

14 Gou L, Xue D, Mou KL, et al. α-MnO_2@In_2O_3 nanotubes as cathode material for aqueous rechargeable Zn-ion battery with high electrochemical performance. J Electrochem Soc, 2019, 166: A3362–A3368

15 Ding Y, Yang IS, Li Z, et al. Nanoporous TiO_2 spheres with tailored textural properties: Controllable synthesis, formation mechanism, and photochemical applications. Prog Mater Sci, 2020, 109: 100620

16 Ding Y, Xu J, Chen L, et al. Pierced ZnO nanosheets via a template-free photopolymerization in microemulsion. J Alloys Compd, 2019, 787: 779–785

17 Liu Q, Wang L, Liu X, et al. N-doped carbon-coated Co_3O_4 nanosheet array/carbon cloth for stable rechargeable Zn-air batteries. Sci China Mater, 2018, 62: 624–632

18 Zhang H, Liu Q, Fang Y, et al. Boosting Zn-ion energy storage capability of hierarchically porous carbon by promoting chemical adsorption. Adv Mater, 2019, 31: 1904948

19 Wu YZ, Ding Y, Hayat T, et al. Enlarged working potential window for MnO_2 supercapacitors with neutral aqueous electrolytes. Appl Surf Sci, 2018, 459: 430–437

20 Li Z, Ding Y, Xiong Y, et al. One-step solution-based catalytic route to fabricate novel α-MnO_2 hierarchical structures on a large scale. Chem Commun, 2005, 7: 918–920

21 Li B, Rong G, Xie Y, et al. Low-temperature synthesis of α-MnO_2 hollow urchins and their application in rechargeable Li^+ batteries. Inorg Chem, 2006, 45: 6404–6410

22 Du Z, Yu P, Wang L, et al. Cubic imidazolate frameworks-derived CoFe alloy nanoparticles-embedded N-doped graphitic carbon for discharging reaction of Zn-air battery. Sci China Mater, 2020, 63: 327–338

23 Hao J, Peng S, Qin T, et al. Fabrication of hybrid Co_3O_4/$NiCo_2O_4$ nanosheets sandwiched by nanoneedles for high-performance supercapacitors using a novel electrochemical ion exchange. Sci China Mater, 2017, 60: 1168–1178

24 Xiong T, Yu ZG, Wu H, et al. Defect engineering of oxygen-deficient manganese oxide to achieve high-performing aqueous zinc ion battery. Adv Energy Mater, 2019, 9: 1803815

25 Fang G, Zhu C, Chen M, et al. Suppressing manganese dissolution in potassium manganate with rich oxygen defects engaged high-energy-density and durable aqueous zinc-ion battery. Adv Funct Mater, 2019, 29: 1808375

26 Galakhov VR, Demeter M, Bartkowski S, et al. Mn 3s exchange splitting in mixed-valence manganites. Phys Rev B, 2002, 65: 113102

27 Zhang N, Cheng F, Liu J, et al. Rechargeable aqueous zinc-manganese dioxide batteries with high energy and power densities. Nat Commun, 2017, 8: 405

28 Zhang N, Jia M, Dong Y, et al. Hydrated layered vanadium oxide as a highly reversible cathode for rechargeable aqueous zinc batteries. Adv Funct Mater, 2019, 29: 1807331

29 Gao X, Wu H, Li W, et al. H^+-insertion boosted α-MnO_2 for an aqueous Zn-ion battery. Small, 2020, 16: 1905842

30 Li H, Han C, Huang Y, et al. An extremely safe and wearable solid-

state zinc ion battery based on a hierarchical structured polymer electrolyte. Energy Environ Sci, 2018, 11: 941–951

31 Islam S, Alfaruqi MH, Mathew V, et al. Facile synthesis and the exploration of the zinc storage mechanism of β-MnO$_2$ nanorods with exposed (101) planes as a novel cathode material for high performance eco-friendly zinc-ion batteries. J Mater Chem A, 2017, 5: 23299–23309

32 Liu Y, Zhou X, Liu R, et al. Tailoring three-dimensional composite architecture for advanced zinc-ion batteries. ACS Appl Mater Interfaces, 2019, 11: 19191–19199

33 Luo S, Xie L, Han F, et al. Nanoscale parallel circuitry based on interpenetrating conductive assembly for flexible and high-power zinc ion battery. Adv Funct Mater, 2019, 29: 1901336

34 Chen L, Yang Z, Qin H, et al. Graphene-wrapped hollow ZnMn$_2$O$_4$ microspheres for high-performance cathode materials of aqueous zinc ion batteries. Electrochim Acta, 2019, 317: 155–163

35 Zhang H, Wang J, Liu Q, et al. Extracting oxygen anions from ZnMn$_2$O$_4$: Robust cathode for flexible all-solid-state Zn-ion batteries. Energy Storage Mater, 2019, 21: 154–161

36 Yuan T, Zhang J, Pu X, et al. Novel alkaline Zn/Na$_{0.44}$MnO$_2$ dual-ion battery with a high capacity and long cycle lifespan. ACS Appl Mater Interfaces, 2018, 10: 34108–34115

37 Qiu N, Chen H, Yang Z, et al. Low-cost birnessite as a promising cathode for high-performance aqueous rechargeable batteries. Electrochim Acta, 2018, 272: 154–160

38 Qin H, Chen L, Wang L, et al. V$_2$O$_5$ hollow spheres as high rate and long life cathode for aqueous rechargeable zinc ion batteries. Electrochim Acta, 2019, 306: 307–316

39 Yang Y, Tang Y, Fang G, et al. Li$^+$ intercalated V$_2$O$_5$·nH$_2$O with enlarged layer spacing and fast ion diffusion as an aqueous zinc-ion battery cathode. Energy Environ Sci, 2018, 11: 3157–3162

40 Yang Q, Mo F, Liu Z, et al. Activating C-coordinated iron of iron hexacyanoferrate for Zn hybrid-ion batteries with 10 000-cycle lifespan and superior rate capability. Adv Mater, 2019, 31: 1901521

41 Chao D, Zhou W, Ye C, et al. An electrolytic Zn-MnO$_2$ battery for high-voltage and scalable energy storage. Angew Chem Int Ed, 2019, 58: 7823–7828

42 Li Y, Wang S, Salvador JR, et al. Reaction mechanisms for long-life rechargeable Zn/MnO$_2$ batteries. Chem Mater, 2019, 31: 2036–2047

43 Huang J, Wang Z, Hou M, et al. Polyaniline-intercalated manganese dioxide nanolayers as a high-performance cathode material for an aqueous zinc-ion battery. Nat Commun, 2018, 9: 2906

Author contributions　　　Wu Y designed and performed the experiments, analyzed the data, and wrote the paper; Tao Y, Zhang X, Zhang K, Chen S, Liu Y, Cai M and Liu X helped to analyze the data; Ding Y and Dai S help to conceive the framework of this paper and review the manuscript. All authors contributed to the general discussion.

Conflict of interest　　　The authors declare no conflict of interest.

Yunzhao Wu obtained his BSc degree from the North China Electric Power University (NCEPU) in 2015. Now he is a PhD candidate in NCEPU under the supervision of Prof. Songyuan Dai. His research interests mainly focus on the advanced electrode materials and charge storage mechanism for ZIBs and supercapacitors.

Yong Ding received his PhD from Hefei Institutes of Physical Science, Chinese Academy of Sciences (CAS) in 2016. After graduation, he became a lecturer in NCEPU. His research interest focuses on the 2D perovskite-based photoelectric devices, including perovskite solar cells and light-emitting diodes.

Songyuan Dai is a professor of the School of Renewable Energy, NCEPU. He obtained his BSc degree in physics from Anhui Normal University in 1987, and MSc and PhD degrees in plasma physics from the Institute of Plasma Physics, CAS in 1991 and 2001, respectively. His research interests mainly focus on the synthesis and application of functional materials and nanomaterials, and the next-generation solar cells including dye sensitized solar cells, quantum dot solar cells and perovskite solar cells.

自组装α-MnO$_2$海胆状微米球应用于水系锌离子电池的高性能阴极

吴云召，陶冶，张先付，张凯，陈盛斌，刘瑜，丁勇[*]，蔡墨郎，刘雪朋，戴松元[*]

摘要　　在绿色能源存储和电动汽车领域，水系锌离子电池(AZIB)是一种十分有潜力的电池技术. α-MnO$_2$作为AZIB的一种热点正极材料，表现出十分优异的电化学性能. 但是，α-MnO$_2$正极的长期稳定性问题仍待解决. α-MnO$_2$材料的结构和形貌会对其性能产生决定性的影响，因此构建多级结构的α-MnO$_2$材料是一种提升AZIB循环充放电性能的可行方法. 本文中，我们采用自组装法合成了一种α-MnO$_2$海胆状微米球(AUM). 这种微米球是由高度结晶的一维α-MnO$_2$纳米线构建而成，这种疏松多孔的结构将有助于提升材料的比表面积和Zn^{2+}离子嵌入的活性位点. 基于AUM的AZIB器件实现了高达308.0 mA h g^{-1}的初始容量，其最大能量密度可达396.7 W h kg^{-1}. 动力学分析表明，AUM正极具备较高比例的电容型容量贡献及快速离子扩散系数. 非原位XRD测试进一步证实，在充放电过程中，存在H$^+$和Zn^{2+}离子的协同嵌入/脱嵌现象. AUM的这种优异特性，使器件实现了很好的电化学性能和循环可逆的结构相变，本工作将有助于高性能AZIB的进一步深入研究.